

The crystal facet-dependent electrochemical performance of TiO₂ nanocrystals for heavy metal detection: theoretical prediction and experimental proof

Jianjun Liao,^{a,b} Fan Yang,^{a,c} Cai-Zhuang Wang,^d Shiwei Lin^{a,c,*}

^a State Key Laboratory of Marine Resource Utilization in South China Sea, Hainan University, Haikou 570228, China

^b Institute of Tropical Agriculture and Forestry, Hainan University, Haikou 570228, China

^c College of Materials and Chemical Engineering, Hainan University, Haikou 570228, China

^d Ames Laboratory-U. S. Department of Energy, and Department of Physics and Astronomy, Iowa State University, Ames, IA 50011, USA

*Address correspondence to: linsw@hainu.edu.cn (S. Lin)

Abstract

Tailored design/fabrication of electroanalytical materials with highly-active exposed crystal planes is of great importance for the development of electrochemical sensing. In this work, combining experimental and theoretical efforts, we reported a facile strategy to fabricate TiO₂ nanocrystals with tunable electrochemical performance for heavy metal detection. Density functional theory (DFT) calculations indicated that TiO₂ (001) facet showed relative larger adsorption energy and lower diffusion energy barrier toward heavy metal ions, which is favorable for obtaining better electrochemical stripping behaviors. Based on this prediction, a series of TiO₂ nanocrystals with different ratios of exposed (001) and (101) facets were synthesized. Electrochemical stripping experiments further demonstrated that with the increase of the percentage of exposed (001) facet, the sensitivity toward Pb(II) and Cd(II) was increased accordingly. When the percentage of exposed (001) facet was increased from 7% to 80%, the sensitivity increased by 190% and 93% for Pb(II) and Cd(II), respectively. Our work provides an effective route to construct advanced electroanalytical materials for sensing.

Keywords:

Crystal facet; Electrochemical detection; Heavy metal ions; Density functional theory

1. Introduction

The increasing of heavy metal pollutants has attracted the public's attention due to its deleterious effect on biological systems [1-3]. Currently, anodic stripping voltammetry has been popularly applied to detect heavy metal ions in water owing to its high sensitivity, accurateness, and low cost [4-7]. To obtain high sensitivity and selectivity, nanostructured metal oxides have been widely employed as modifiers of the working electrodes [8-11]. The detection strategy stems from the selective adsorption properties of modifiers [12]. Unfortunately, the increased sensing performance is simply attributed to the large surface area and rich active sites [13,14]. Few studies provide insightful information from atomic level on the interaction between metal ions and material surfaces.

Crystal plane is an important factor related to the physicochemical properties of materials because the facet-dependent properties intrinsically arise from the arrangement manner of surface atoms and dangling bonds on the exposed surface [15-18]. Thus, even if some materials have identical chemical compositions but different exposed facets may show quite different performances. To date, crystal plane effects have gained great interest in lots of fields, such as photocatalysts [19-20], solar cell [21,22], electrochemical energy storage [23,24], and so on. However, to the best of our knowledge, only a few studies have been focused on the facet-dependent electrochemical performances toward heavy metal ions detection [7,9,25-27]. For instance, Xin-jiu Huang research group found that Cu_2O microcrystals with different facets showed different sensitivity in the determination of lead ions, following the sequence $(111) > (100) > (110)$ [25]. Furthermore, facet-dependent electrochemical behaviors were also observed on other metal oxides, like, SnO_2 [26], Fe_3O_4 [9], and Fe_2O_3 [27]. Although experimental studies have been demonstrated the effect of crystal facets on the detection of heavy metal ions, the atomistic understanding of the mechanism of the electroanalytical behaviors is far from satisfactory. Therefore, the conception of this work is to design a rational structure of modifier based on

first-principles theoretical prediction, and then experimentally synthesize and prove its electroanalytical performance.

TiO₂ is an extensively studied semiconductor material. It is usually exposed to low index facets such as (001) and (101) [23]. The facet-dependent performance has been deeply investigated in term of surface structure, computational and experimental science [28-31]. Moreover, the synthesis technology of TiO₂ nanocrystals with specific facets is relatively rich and mature. Therefore, TiO₂ nanocrystals are selected as a typical example to investigate their facet-dependent stripping behaviors toward heavy metal ions, including three aspects: (i) first-principles theoretical calculations of adsorption/desorption behaviors of metal atoms on TiO₂ (001) and (101) facets; (ii) controlled the synthesis of TiO₂ nanocrystals with different ratios of (001) and (101) facets; (iii) characterization of the stripping behaviors of the as-prepared TiO₂ nanocrystals and experimental proof of the facet-dependent electroanalytical properties. More importantly, the obtained results are helpful for us to understand the structure-performance relationship and improve the efficiency of nanostructured materials in electroanalysis.

2. Experimental Section

2.1. Synthesis of TiO₂ nanocrystals with different facets dominated percentage

TiO₂ nanocrystals were synthesized by hydrothermal method according to a previous report [32]. 10 mL Titanium butoxide (Ti(OC₄H₉)₄) and different volume of hydrofluoric acid solution (0 mL, 1.5 mL, 3 mL) were mixed in a Teflon-lined autoclave, then kept at 180 °C for 24 h. The volume of HF solution was varied from 0 mL to 3 mL to control the percentage of exposed (001) facet. According to HF volume used, the as-prepared samples were denoted as HF0, HF1.5, and HF3, respectively. After hydrothermal treatment, the white precipitates were collected and washed with distilled water several times and dried in an oven at 80 °C.

2.2. Material characterization

The morphology of TiO₂ nanocrystals was observed on a field-emission scanning electron microscope (FESEM, Hitachi S-4800) and Transmission electron microscopy

(TEM, JEOL JEM-2010). The crystal structure of the samples was examined using X-ray diffraction (XRD, Bruker D8) with Cu K α radiation.

2.3. Electrode fabrication

4 mg of TiO₂ nanocrystals was dissolved in 1 mL of ethanol and sonicated for 30 min. Before modification, the glassy carbon electrode (GCE) was sequentially polished with alumina powder slurries to a mirror shiny surface. Then, 3 μ L of the suspension was dropped onto GCE surface. With the solvent completely evaporated at room temperature, TiO₂ modified electrodes were obtained.

2.4. Electrochemical measurements

Square wave anodic stripping voltammetry (SWASV) was measured with an electrochemical analyzer CHI660E (ChenHua Instruments Co., Shanghai, China). The three-electrode system was composed of TiO₂ modified electrode, Ag/AgCl electrode and platinum wire as the working, reference and counter electrodes, respectively. For the accumulation step, targeted ions were deposited to the working surface at the potential of -1.0 V for 150 s. The SWASV parameters were 15 Hz frequency, 25 mV amplitude, and 4 mV step potential. After each test, the working electrode was regenerated at 0 V for 150 s under stirring.

2.5. Computational details

Density function theory (DFT) calculations were performed by Vienna ab-initio simulation package (VASP) [33,34]. The generalized gradient approximation (GGA) in the Perdew-Burke-Ernzerhof (PBE) form was chosen as the exchange-correlation potential. The 4 \times 4 \times 1 k-point mesh was applied to sample the Brillouin zone. The energy cutoff was set to be 500 eV. The atomic positions are relaxed until the forces were converged to 0.02 eV/Å. To model the surface, we used periodically repeated slabs separated by a vacuum of \sim 15 Å width. Anatase TiO₂ with two different surfaces was considered in this work. For TiO₂ (001) surface, a (2 \times 2) supercell with 48 atoms was adopted (Figure 1a). For TiO₂ (101) surface, a (1 \times 2) supercell with 72 atoms was adopted (Figure 1b).

The adsorption energy (E_{ads}) is defined as $E_{ads} = E_{atom+slab} - (E_{slab} + E_{atom})$, where $E_{atom+slab}$, E_{slab} and E_{atom} are the energies of the metal atom adsorbed on slab system, isolated slab surface, and isolated metal atom, respectively. Under this definition, the more negative value stands for the more energetically stable adsorption.

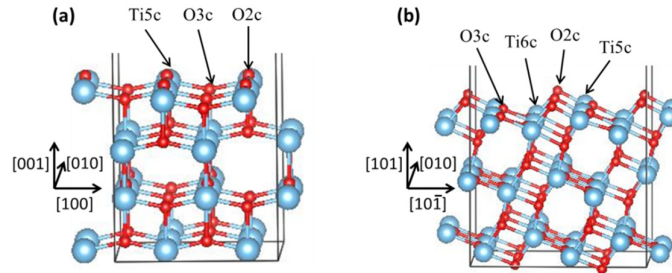


Figure 1. Slab models for anatase TiO_2 (a) (001) and (b) (101) facets. Ti: large/blue spheres. O: small/red spheres. O2c, O3c, Ti5c, and Ti6c are denoted as 2-fold-coordinate O atom, 3-fold-coordinate O atom, 5-fold-coordinate Ti atom, and 6-fold-coordinate Ti atom, respectively.

3. Results and Discussion

3.1. Theoretical DFT calculation

3.1.1 Adsorption energies and bond lengths calculation

First-principles calculations based on DFT were used to investigate the adsorption behaviors of metal atoms on anatase TiO_2 (001) and (101) facets. Table 1 lists the adsorption energies (E_{ad}) and bond lengths of the most stable adsorption configurations. Compared the adsorption energies of Pb/ TiO_2 (001) adsorption systems with those of Cd/ TiO_2 (001) systems, it can be found that (001) facet exhibited stronger adsorption capacity toward Pb than Cd. Similar results can be also found on (101) facet. Meanwhile, the different facet of TiO_2 showed the different adsorption capacity toward the same metal atom. In detail, the adsorption energy of Pb on (001) facet was -2.59 eV, which is larger than that of Pb on (101) facet (-2.35 eV). A larger adsorption energy can be also observed on Cd/ TiO_2 (001) system (-0.48 eV) when compared with that of Cd/ TiO_2 (101) system (-0.13 eV). Above results

indicate that TiO₂ (001) surface is more reactive and easy to bond with metal atoms, which can be further proved by the bond length analysis shown in Figure 2.

Table 1. Optimized structural parameters and adsorption energies for metal atoms adsorbed on TiO₂ exposed (001) and (101) facets.

	(001)		(101)	
	Pb	Cd	Pb	Cd
E _{ad} (eV)	-2.59	-0.48	-2.35	-0.13
Bond length (Å)	Pb-O2c 2.30, 2.30	Cd-O2c 3.50 Cd-O3c 3.48	Pb-O2c 2.23, 2.26 Pb-O3c 2.35	Cd-O2c 3.50, 3.58 Cd-O3c 3.52

Figure 2 shows the optimized adsorption configurations of heavy metal atoms on (001) and (101) facets. For both (001) and (101) facets, the bond lengths of Pb-O were obviously shorter than those of Cd-O. The short bond length is recognized as strong interaction with TiO₂ surface, which is consistent with the results of adsorption energies shown in Table 1. However, because of the different atomic density distribution on (001) and (101) facets, metal atoms were only bonded with adjacent two oxygen atoms of (001) facet, and tended to bond with adjacent three oxygen atoms of (101) facet. We suspected that the extra Pb/Cd-O bond formed on (101) facet may make desorption behavior difficulty and weaken the stripping signal, which will be further discussed below.

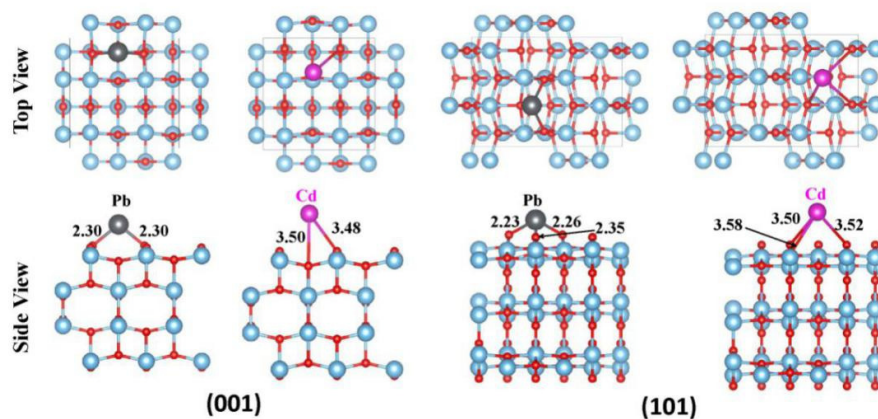


Figure 2. Top/side views of optimized adsorption configurations of heavy metal atoms on TiO₂ exposed (001) and (101) facets. Ti: large/blue spheres. O: small/red spheres.

3.1.2 DOS analysis

The interaction details of heavy metal atoms absorption on the substrate can be further observed from the Density of states (DOS). Figure 3 compares the DOS of Pb/Cd absorbed on TiO₂ (001) and (101) facets. As shown in Figure 3a,b, before Pb/Cd adsorption, Fermi levels of TiO₂ (001) and (101) facets located at the top of valence band. After Pb adsorption, Fermi levels of TiO₂ (001) and (101) facets shifted to the bottom of conduction band, indicating the strong chemical bonding (Figure 3c,d). Furthermore, it can be seen from Figure 3c that there was a hybrid peak at -0.33 eV in Pb/TiO₂ (001) system, which was induced by the hybridization of O2p and Pb 6p orbits. While such a hybrid peak cannot be observed from Pb/TiO₂ (101) system (Figure 3d). The newborn hybrid peak demonstrated that the absorption energy of Pb/TiO₂ (001) system was stronger than that of Pb/TiO₂ (101) system. A similar phenomenon can be also observed in Cd absorption system. As shown in Figure 3e,f, there was a hybrid peak located near Fermi level of Cd/TiO₂ (001) system, but not existed on Cd/TiO₂ (101) system.

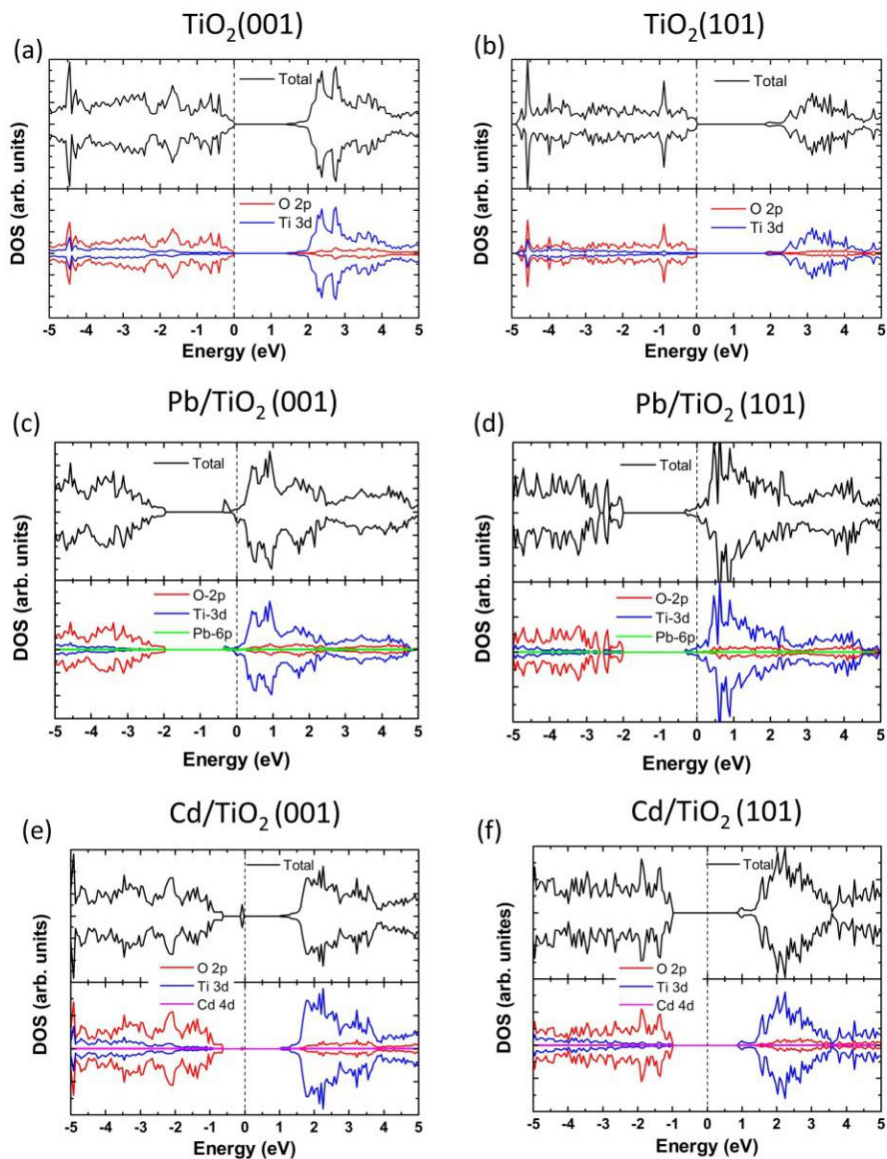


Figure 3. DOS of Pb and Cd atoms adsorbed on TiO_2 (001) and (101) facets: (a) and (b) are DOS of TiO_2 (001) and (101) facets, respectively. (c) and (d) are Pb adsorption on TiO_2 (001) and (101), respectively. (e) and (f) are Cd adsorption on TiO_2 (001) and (101), respectively.

3.1.3 Diffusion energy barrier analysis

The diffusion energy barriers of Pb/Cd on TiO_2 (001) and (101) facets were analyzed with CI-NEB method, and the diffusion paths were depicted in Figure S1 in Supporting Information. As shown in Figure 4, the diffusion energy barriers of Pb on

TiO₂ (001) and (101) facets were predicted to be 0.92 eV and 1.30 eV, respectively, while the diffusion energy barriers of Cd on TiO₂ (001) and (101) facets were predicted to be 0.06 eV and 0.09 eV, respectively. The results indicate that Pb/Cd can diffuse easier on TiO₂ (001) facet than that on TiO₂ (101) facet, leading to the enhanced electrochemical signals. The relative high diffusion energy barrier can be ascribed to extra Pb/Cd-O bond formed on TiO₂ (101) facet, which is supported by the stable adsorption configurations (Figure 2).

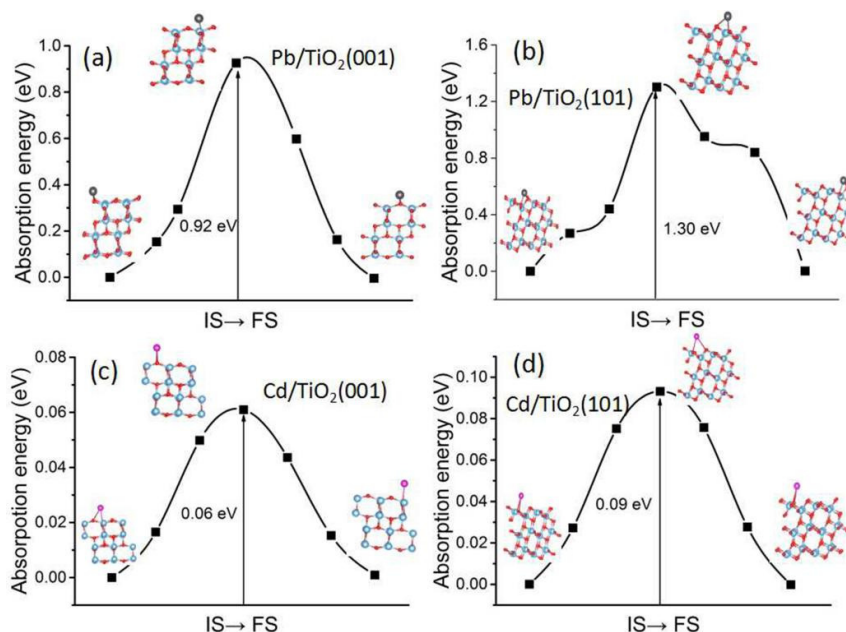
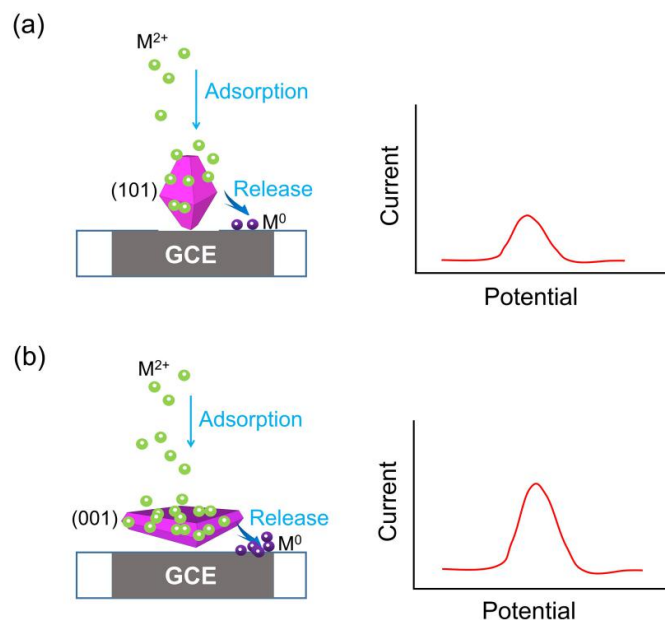


Figure 4. Transition-state (TS) barriers of (a,b) Pb(II) and (c,d) Cd(II) on TiO₂ (001) and (101) facets. The insets represent the optimized stable adsorption and TS structures. IS: initial state, FS: final state.

3.2 Optimal exposed facet suggested by DFT calculation

Adsorption-release model is often used to describe the stripping voltammetric technique [35]. Scheme 1 illuminates how adsorption-release process affects the heavy metal ions sensing on the TiO₂ (001) and (101) facets. Due to the relative high adsorption energy and low diffusion energy barrier of TiO₂ (001) facet, large amounts of metal ions can be adsorbed onto the (001) facet, and then effectively diffuse to the GCE surface, thus strengthen the stripping current signal.

In this case, adsorption energy has a closed relationship with the exposed facet on TiO₂, following the order (001) > (101). Preliminarily, it is predicted that (001) facet shows better stripping behavior toward heavy metal ions when compared with (101) facet. Further analysis of other descriptors (bond length, DOS, and diffusion energy barrier) supports our speculation: in order to maximize the detection sensitivity of heavy metal ions, the exposed percentage of (001) facets should be as high as possible in TiO₂ nanocrystals.



Scheme 1. Schematic diagrams illuminate how adsorption-release process affects the heavy metal ions sensing at TiO₂ (001) and (101) facets.

3.3. Experimental proof

3.3.1 Material preparation

In order to check above prediction, a series of TiO₂ nanocrystals with different ratios of the exposed (001) and (101) facets were carefully synthesized. The percentage of (001) facets was calculated according to Figure S2 in Supporting Information. Figure 5a-c illustrates the percentage of exposed (001) facets in TiO₂ nanocrystals increases with the increasing amount of HF. When no HF was added, the as-prepared samples (designated as HF0) showed truncated bipyramidal structure, which was enclosed by eight (101) facets and two (001) facets (Figure 5g)

[36,37]. The percentage of exposed (001) facets was about 7%. When 1.5 mL HF was added into the precursor, the as-prepared samples (named HF1.5) became stocky, and the percentage of exposed (001) facets was increased to 35% (Figure 5h). This is because fluorine ions are efficient capping agents, which are favorable for the growth of (001)-faceted surfaces [31,38,39]. As shown in Figure 5i, further increasing the volume of HF to 3 mL resulted in rectangle TiO₂ nanosheets with up to 80% of (001) facets (noted as HF3).

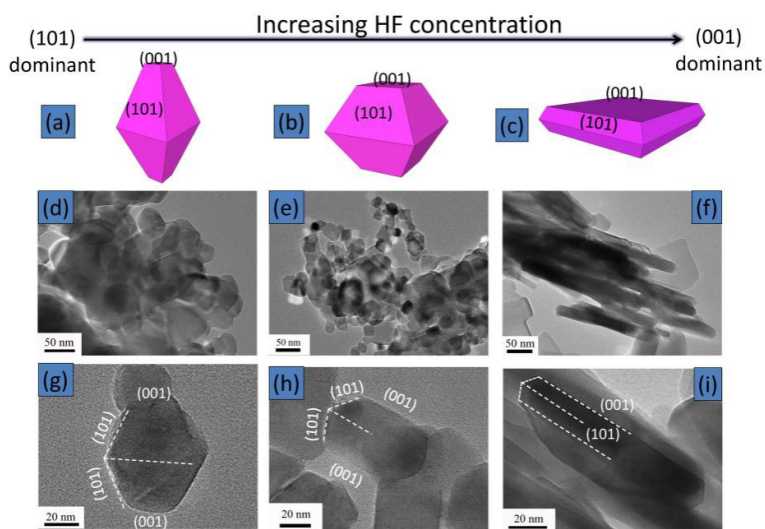


Figure 5. (a), (b) and (c) are the schematic diagrams of HF0, HF1.5 and HF3 samples. (d), (e) and (f) are the TEM images of HF0, HF1.5, and HF3 samples, respectively. (g), (h) and (i) are the enlarged TEM images of HF0, HF1.5, and HF3 samples, respectively.

3.3.2 Individual detection of Pb(II) and Cd(II) on the different facets

In order to exclude the influence of crystalline phase on the stripping behavior, all the samples were calcined at the same temperature 500 °C. XRD patterns (Figure S3) show that HF0, HF1.5, and HF3 are pure anatase. The electroanalysis properties of the as-prepared TiO₂ nanocrystals with different ratios of the exposed (001) facets were further evaluated by SWASV. Prior to stripping analysis, the experimental conditions, including deposition potential, deposition time, and pH values of supporting electrolyte, were first selected according to Figure S4.

Under the optimal experimental conditions, Figure 6 shows the SWASV responses of HF0, HF1.5 and HF3 samples toward Pb(II) and Cd(II). The current density (j , $\mu\text{A}/\text{cm}^2$) was employed in order to exclude the effect of electrode active area on electrochemical measurements (Figure S5). As seen, the current densities increased linearly with increasing the concentrations of Pb(II) and Cd(II). The corresponding linearization equations were summarized in Table S1. The detection sensitivities of Pb(II) are 143.97, 296.72, and 417.12 $\mu\text{A } \mu\text{M}^{-1} \text{cm}^2$ for HF0, HF1.5, and HF3, respectively. That is, the sensitivity of HF3 is about 1.4 times that of HF1.5, and about 2.9 times that of HF0. For Cd(II) detection, the sensitivity of HF3 is 243.33 $\mu\text{A } \mu\text{M}^{-1} \text{cm}^2$, which is about 1.3 times that of HF1.5 (187.09 $\mu\text{A } \mu\text{M}^{-1} \text{cm}^2$), and about 1.9 times that of HF0 (125.95 $\mu\text{A } \mu\text{M}^{-1} \text{cm}^2$).

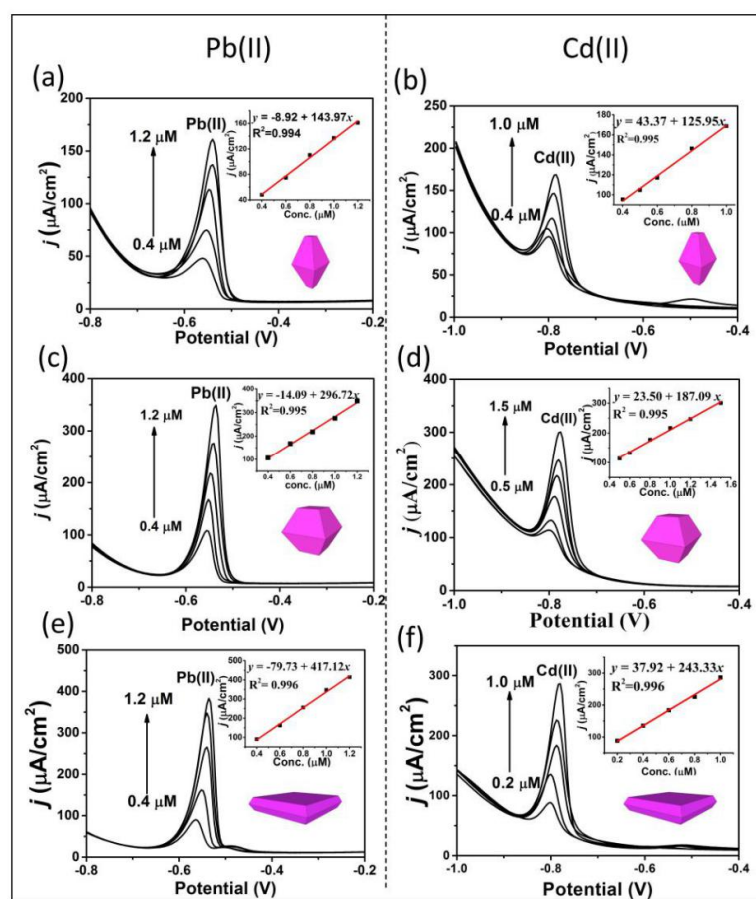


Figure 6. SWASV responses of HF0, HF1.5, and HF3 modified GCE in the presence of Pb(II) and Cd(II) ions. The insets show the corresponding calibration curves.

For clear, the histogram of sensitivities was drawn on Figure 7. Either for Pb(II) or Cd(II), the order of sensitivity was found to follow the sequence: HF3 > HF1.5 > HF0, indicating that the exposed crystal facets have a close relationship with stripping behaviors [40,41]. With the increase of the percentage of exposed (001) facets, the electrochemical sensitivity was increased accordingly. When the percentage of exposed (001) facets was increased to 80%, the sensitivity reached a maximum, about 190% and 93% enhancement for Pb(II) and Cd(II), respectively.

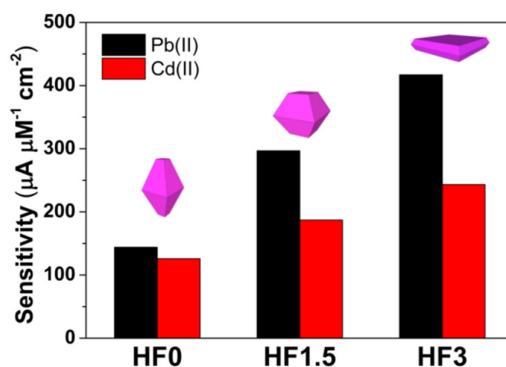


Figure 7. Comparison of the sensitivity of HF0, HF1.5, and HF3 modified GCE.

Comparison of the sensitivities of different modifiers with different facets for SWASV responses of heavy metal ions is summarized in Table 2. Most of the previous works focused on the metal oxides, like Fe₃O₄, Cu₂O, Fe₂O₃ and SnO₂. Although the analytical performance of TiO₂ (001) facet is not the best, our work can provide an effective way to realize the rational design of electrochemical sensing materials in the future.

Table 2. Comparison of sensitivities of different modifiers with different facets for SWASV responses of heavy metal ions

Modifier	Facet	Heavy metal ions	Sensitivity ($\mu\text{A } \mu\text{M}^{-1} \text{ cm}^{-2}$)	Ref.
Fe ₃ O ₄	(100)	Pb(II)	235.97	[9]
	(111)		1577.6	
	(100)		127	[25]
Cu ₂ O	(110)	Pb(II)	90.1	
	(111)		178	
	(110)		572.1	[27]
Fe ₂ O ₃	(001)	Pb(II)	85.6	
	(012)		17.8	
SnO ₂	(221)	Pb(II)	85.54	[26]
	(110)		338.92	
TiO ₂	(001)	Pb(II)	417.12	
			143.97	
	(101)		Cd(II)	243.33
		125.95		

3.3.3. Simultaneous detection of Pb(II) and Cd(II) on the same facets

Individual measurements of Pb(II) and Cd(II) demonstrated that the different crystal facet showed different sensing performance toward heavy metal ions (Figure 6). Next, we investigated the different heavy metal sensing performance on the same crystal facet. Figure 8a shows the SWASV responses of HF3 modified GCE electrodes for the simultaneous analysis of Pb(II) and Cd(II) ions. Pb(II) and Cd(II) were detected at potentials of -0.55 V and -0.78 V, respectively. The increase of peak currents was obtained when simultaneously increasing the concentration of Pb(II) and Cd(II). As shown in Figure 8b, the linearization equations were $y = -8.90 + 744.50x$ and

$y=2.72+452.06x$ for Pb(II) and Cd(II), respectively. The sensitivity of Pb(II) ($744.50 \mu\text{A } \mu\text{M}^{-1} \text{cm}^{-2}$) is about 1.6 times larger than that of Cd(II) ($452.06 \mu\text{A } \mu\text{M}^{-1} \text{cm}^{-2}$). The different sensitivities toward Pb(II) and Cd(II) reflect the difference of adsorption and desorption abilities on TiO_2 (001) facet, which is reasonable according to the above theoretical calculation.

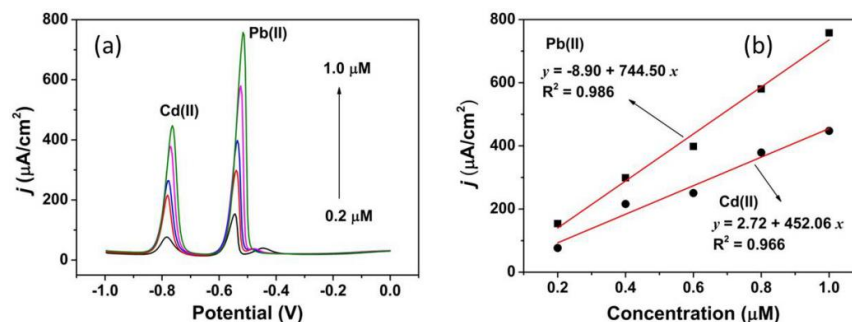


Figure 8. (a) SWASV responses of HF3 modified GCE electrodes for the simultaneous analysis of Pb(II) and Cd(II) ions; (b) shows the corresponding calibration curves.

3.4. Interference study

There are various metal ions coexisted in the real water environment, which may cause interference with our system. Therefore, the interference study was evaluated by adding some possible metal ions in the detection of Pb(II) and Cd(II). The experimental results (not shown here) indicated that 100 times of K^+ , Na^+ , Ba^{2+} , Ca^{2+} , Cl^- , and SO_4^{2-} had no significant influence on the signals of Pb(II) and Cd(II), the change of peak currents was within $\pm 10\%$ tolerance ratio. 10 times of Zn^{2+} , Mg^{2+} , Fe^{2+} , Ni^{2+} , and Co^{2+} did not affect the determination of Pb(II) and Cd(II). The equal concentration of Hg^{2+} and Cu^{2+} obviously affected the stripping signals of Pb(II) and Cd(II), the change of peak currents exceeded 20%.

3.5. Real Sample Analysis

Practical evaluation of the modified electrodes was performed via testing a real water sample, which was taken from Nandu Jiang River in Haikou city. Before measurements, the water sample was filtered so as to remove any large particulates and then diluted with 0.1 M NaAc-HAc buffer solution (pH 5.0) in the ratio of 1:1. Standard addition method was used and the SWASV response curves are shown in

Figure S6 in Supporting Information. In order to verify the accuracy of this method, the results obtained by this method were compared with those by ICP-MS. As shown in Table 3, the concentration of Pb(II) in the real sample was about 38.7 nM. The relative error was 5.66% when compared with the result by ICP-MS. Therefore, the modified electrode has practical application potential.

Table 3 Comparison of HF3 modified electrodes and ICP-MC methods for the determination of Pb(II) and Cd(II) ions in a real sample.

Ions	Detected by this method (nM)	ICP-MC (nM)	Relative error (%)
Pb(II)	38.7	41.02	5.66
Cd(II)	Not detected	Not detected	--

4. Conclusions

In conclusion, through engineering the different ratios of exposed (001) and (101) facets on TiO₂ nanocrystals, crystal facet-dependent electrochemical performance has been investigated experimentally and theoretically. The calculation results indicated that in order to maximize the detection sensitivity of heavy metal ions, the exposed percentage of (001) facet should be as high as possible in TiO₂ nanocrystals. The experimental results verify the theoretical calculation well. When the percentage of exposed (001) facet was increased from 7% to 80%, the sensitivity increased by 190% and 93% for Pb(II) and Cd(II), respectively. The enhanced performance of (001) dominated TiO₂ nanocrystals is derived from the increased adsorption capacity and the low diffusion energy barrier of (001) facet, which are rationalized by the theoretical prediction. The crystal facet engineering strategy demonstrated in the present work can provide an effective way to realize the rational design of electrochemical sensing materials in the future.

Acknowledgment

This work is supported by the Natural Science Foundation of Hainan Province (517027), the Key Research and Development Program of Hainan Province

(ZDYF2017166), and Scientific Research Foundation of Hainan University (kyqd1659). Work at Ames Laboratory was supported by the US Department of Energy, Basic Energy Sciences, Division of Materials Science and Engineering under Contract No. DE-AC02-07CH11358, including a grant of computer time at the National Energy Research Scientific Computing Centre (NERSC) in Berkeley, CA.

References

- [1] Y. Wassana, L. Yuehe, H. Kitiya, E.F. Glen, A. Raymond, C. Timchalk, Electrochemical Sensors for the Detection of Lead and Other Toxic Heavy Metals: The Next Generation of Personal Exposure Biomonitoring, *Environmental Health Perspectives*, 115(2007) 1683-1690.
- [2] S. Su, W. Wu, J. Gao, J. Lu, C. Fan, Nanomaterials-based sensors for applications in environmental monitoring, *Journal of Materials Chemistry*, 22(2012) 18101-18110.
- [3] S. Lee, J. Oh, D. Kim, Y. Piao, A sensitive electrochemical sensor using an iron oxide/graphene composite for the simultaneous detection of heavy metal ions, *Talanta*, 160(2016) 528-536.
- [4] I. Rutyna, M. Korolczuk, Determination of lead and cadmium by anodic stripping voltammetry at bismuth film electrodes following double deposition and stripping steps, *Sensors and Actuators B: Chemical*, 204(2014) 136-141.
- [5] L. Zhu, L. Xu, B. Huang, N. Jia, L. Tan, S. Yao, Simultaneous determination of Cd(II) and Pb(II) using square wave anodic stripping voltammetry at a gold nanoparticle-graphene-cysteine composite modified bismuth film electrode, *Electrochimica Acta*, 115(2014) 471-477.
- [6] W.-Y. Zhou, J.-Y. Liu, J.-Y. Song, J.-J. Li, J.-H. Liu, X.-J. Huang, Surface-Electronic-State-Modulated, Single-Crystalline (001) TiO₂ Nanosheets for Sensitive Electrochemical Sensing of Heavy-Metal Ions, *Analytical Chemistry*, 89(2017) 3386-3394.
- [7] P.-H. Li, Y.-X. Li, S.-H. Chen, S.-S. Li, M. Jiang, Z. Guo, et al., Sensitive and interference-free electrochemical determination of Pb(II) in wastewater using porous Ce-Zr oxide nanospheres, *Sensors and Actuators B: Chemical*, 257(2018) 1009-1020.
- [8] X.-Y. Yu, X.-Z. Yao, T. Luo, Y. Jia, J.-H. Liu, X.-J. Huang, Facile Synthesis of Urchin-like NiCo₂O₄ Hollow Microspheres with Enhanced Electrochemical

Properties in Energy and Environmentally Related Applications, ACS Applied Materials & Interfaces, 6(2014) 3689-3695.

[9] X.-Z. Yao, Z. Guo, Q.-H. Yuan, Z.-G. Liu, J.-H. Liu, X.-J. Huang, Exploiting Differential Electrochemical Stripping Behaviors of Fe₃O₄ Nanocrystals toward Heavy Metal Ions by Crystal Cutting, ACS Applied Materials & Interfaces, 6(2014) 12203-12213.

[10] Y. Wei, C. Gao, F.-L. Meng, H.-H. Li, L. Wang, J.-H. Liu, et al., SnO₂/Reduced Graphene Oxide Nanocomposite for the Simultaneous Electrochemical Detection of Cadmium(II), Lead(II), Copper(II), and Mercury(II): An Interesting Favorable Mutual Interference, The Journal of Physical Chemistry C, 116(2011) 1034-1041.

[11] Q.-X. Zhang, D. Peng, X.-J. Huang, Effect of morphology of α -MnO₂ nanocrystals on electrochemical detection of toxic metal ions, Electrochemistry Communications, 34(2013) 270-273.

[12] L. Wang, W.-H. Xu, R. Yang, T. Zhou, D. Hou, X. Zheng, et al., Electrochemical and Density Functional Theory Investigation on High Selectivity and Sensitivity of Exfoliated Nano-Zirconium Phosphate toward Lead(II), Analytical Chemistry, 85(2013) 3984-3990.

[13] R.-X. Xu, X.-Y. Yu, C. Gao, Y.-J. Jiang, D.-D. Han, J.-H. Liu, et al., Non-conductive nanomaterial enhanced electrochemical response in stripping voltammetry: The use of nanostructured magnesium silicate hollow spheres for heavy metal ions detection, Analytica Chimica Acta, 790(2013) 31-38.

[14] C. Gao, X.-Y. Yu, R.-X. Xu, J.-H. Liu, X.-J. Huang, AlOOH-Reduced Graphene Oxide Nanocomposites: One-Pot Hydrothermal Synthesis and Their Enhanced Electrochemical Activity for Heavy Metal Ions, ACS Applied Materials & Interfaces, 4(2012) 4672-4682.

[15] Y. Wang, X. Yang, J. Bai, X. Jiang, G. Fan, High sensitivity hydrogen peroxide and hydrazine sensor based on silver nanocubes with rich {100} facets as an enhanced electrochemical sensing platform, Biosensors and Bioelectronics, 43(2013) 180-185.

[16] C. Wang, D. Cai, B. Liu, H. Li, D. Wang, Y. Liu, et al., Ethanol-sensing performance of tin dioxide octahedral nanocrystals with exposed high-energy {111} and {332} facets, Journal of Materials Chemistry A, 2(2014) 10623-10668.

- [17] A. Gurlo, Nanosensors: towards morphological control of gas sensing activity. SnO₂, In₂O₃, ZnO and WO₃ case studies, *Nanoscale*, 3(2011) 154-165.
- [18] S.-C. Wu, C.-S. Tan, M.H. Huang, Strong Facet Effects on Interfacial Charge Transfer Revealed through the Examination of Photocatalytic Activities of Various Cu₂O-ZnO Heterostructures, *Advanced Functional Materials*, (2017) DOI:10.1002/adfm.201604635.
- [19] G. Liu, J.C. Yu, G.Q. Lu, H.-M. Cheng, Crystal facet engineering of semiconductor photocatalysts: motivations, advances and unique properties, *Chemical Communications*, 47(2011) 6763-6783.
- [20] L. Jing, W. Zhou, G. Tian, H. Fu, Surface tuning for oxide-based nanomaterials as efficient photocatalysts, *Chemical Society Reviews*, 42(2013) 9509-9549.
- [21] J.-D. Peng, P.-C. Shih, H.-H. Lin, C.-M. Tseng, R. Vittal, V. Suryanarayanan, et al., TiO₂ nanosheets with highly exposed (001)-facets for enhanced photovoltaic performance of dye-sensitized solar cells, *Nano Energy*, 10(2014) 212-221.
- [22] C. Chen, Y. Ikeuchi, L. Xu, G.A. Sewvandi, T. Kusunose, Y. Tanaka, et al., Synthesis of [111]- and {010}-faceted anatase TiO₂ nanocrystals from tri-titanate nanosheets and their photocatalytic and DSSC performances, *Nanoscale*, 7(2015) 7980-7991.
- [23] F. Wang, X. Wang, Z. Chang, Y. Zhu, L. Fu, X. Liu, et al., Electrode materials with tailored facets for electrochemical energy storage, *Nanoscale Horiz*, 1(2016) 272-289.
- [24] G. Longoni, R.L. Pena Cabrera, S. Polizzi, M. D'Arienzo, C.M. Mari, Y. Cui, et al., Shape-Controlled TiO₂ Nanocrystals for Na-Ion Battery Electrodes: The Role of Different Exposed Crystal Facets on the Electrochemical Properties, *Nano Letters*, 17(2017) 992-1000.
- [25] Z.-G. Liu, Y.-F. Sun, W.-K. Chen, Y. Kong, Z. Jin, X. Chen, et al., Facet-Dependent Stripping Behavior of Cu₂O Microcrystals Toward Lead Ions: A Rational Design for the Determination of Lead Ions, *Small*, 11(2015) 2493-2498.
- [26] Z. Jin, M. Yang, S.-H. Chen, J.-H. Liu, Q.-X. Li, X.-J. Huang, Tin Oxide Crystals Exposed by Low-Energy {110} Facets for Enhanced Electrochemical Heavy Metal Ions Sensing: X-ray Absorption Fine Structure Experimental Combined with Density-Functional Theory Evidence, *Analytical Chemistry*, 89(2017) 2613-2621.

- [27] W.-H. Xu, Q.-Q. Meng, C. Gao, J. Wang, Q.-X. Li, J.-H. Liu, et al., Investigation of the facet-dependent performance of α -Fe₂O₃ nanocrystals for heavy metal determination by stripping voltammetry, *Chemical Communications*, 50(2014) 5011-5013.
- [28] J. Pan, G. Liu, G.Q. Lu, H.-M. Cheng, On the True Photoreactivity Order of {001}, {010}, and {101} Facets of Anatase TiO₂ Crystals, *Angewandte Chemie International Edition*, 50(2011) 2133-2137.
- [29] Q. Wu, M. Liu, Z. Wu, Y. Li, L. Piao, Is Photooxidation Activity of {001} Facets Truly Lower Than That of {101} Facets for Anatase TiO₂ Crystals?, *The Journal of Physical Chemistry C*, 116(2012) 26800-26804.
- [30] N. Roy, Y. Sohn, D. Pradhan, Synergy of Low-Energy {101} and High-Energy {001} TiO₂ Crystal Facets for Enhanced Photocatalysis, *ACS Nano*, 7(2013) 2532-2540.
- [31] O. Lamiel-Garcia, D. Fernandez-Hevia, A.C. Caballero, F. Illas, Adsorption properties of trifluoroacetic acid on anatase (101) and (001) surfaces: a density functional theory study, *Physical Chemistry Chemical Physics*, 17(2015) 23627-23633.
- [32] H.G. Yang, C.H. Sun, S.Z. Qiao, J. Zou, G. Liu, S.C. Smith, et al., Anatase TiO₂ single crystals with a large percentage of reactive facets, *Nature*, 453(2008) 638-41.
- [33] G. Kresse, J. Furthmüller, Efficiency of ab-initio total energy calculations for metals and semiconductors using a plane-wave basis set, *Computational Materials Science*, 6(1996) 15-50.
- [34] G. Kresse, J. Furthmüller, Efficient iterative schemes for ab initio total-energy calculations using a plane-wave basis set, *Physical Review B*, 54(1996) 11169-11186.
- [35] S.-S. Li, W.-J. Li, T.-J. Jiang, Z.-G. Liu, X. Chen, H.-P. Cong, et al., Iron Oxide with Different Crystal Phases (α - and γ -Fe₂O₃) in Electroanalysis and Ultrasensitive and Selective Detection of Lead(II): An Advancing Approach Using XPS and EXAFS, *Analytical Chemistry*, 88(2016) 906-914.
- [36] A. Selloni, Crystal growth: Anatase shows its reactive side, *Nat Mater*, 7(2008) 613-615.
- [37] G. Liu, H.G. Yang, J. Pan, Y.Q. Yang, G.Q. Lu, H.-M. Cheng, Titanium Dioxide Crystals with Tailored Facets, *Chemical Reviews*, 114(2014) 9559-9612.

- [38] W.-J. Ong, L.-L. Tan, S.-P. Chai, S.-T. Yong, A.R. Mohamed, Highly reactive {001} facets of TiO₂-based composites: synthesis, formation mechanism and characterization, *Nanoscale*, 6(2014) 1946-2008.
- [39] Q. Kuang, X. Wang, Z. Jiang, Z. Xie, L. Zheng, High-Energy-Surface Engineered Metal Oxide Micro- and Nanocrystallites and Their Applications, *Accounts of Chemical Research*, 47(2014) 308-318.
- [40] J. Long, S. Wang, H. Chang, B. Zhao, B. Liu, Y. Zhou, et al., Bi₂MoO₆ Nanobelts for Crystal Facet-Enhanced Photocatalysis, *Small*, 10(2014) 2791-2795.
- [41] J. Xu, Z. Xue, N. Qin, Z. Cheng, Q. Xiang, The crystal facet-dependent gas sensing properties of ZnO nanosheets: Experimental and computational study, *Sensors and Actuators B: Chemical*, 242(2017) 148-157.